Reliability Engineering and System Safety 250 (2024) 110267

Contents lists available at ScienceDirect

Reliability Engineering and System Safety

journal homepage: www.elsevier.com/locate/ress

A general approach to assessing SHM reliability considering sensor failures based on information theory

Wen Wu [a,*], Sergio Cantero-Chinchilla [c], Darren Prescott [b], Rasa Remenyte-Prescott [b], Manuel Chiachío [d]

[a] Institute for Aerospace Technology & Resilience Engineering Research Group, The University of Nottingham, NG7 2RD, United Kingdom
[b] Resilience Engineering Research Group, Faculty of Engineering, University of Nottingham, University Park, Nottingham, NG7 2RD, United Kingdom
[c] School of Electrical, Electronic and Mechanical Engineering, University of Bristol, Bristol, BS8 1TR, UK
[d] Department of Structural Mechanics and Hydraulic Engineering, Andalusian Research Institute in Data Science and Computational Intelligence (DaSCI), University of Granada (UGR), Granada 18001, Spain

ARTICLE INFO

Keywords:
Monitoring system reliability
Structural health monitoring
Bayesian inverse problem
Kullback–Leibler divergence
Petri nets
Time of flight
Scattering coefficients

ABSTRACT

Structural health monitoring systems (SHM) involve implementing damage identification strategies to determine the health state of structures. However, it is important to pay close attention to the system degradation, especially the effect of sensor degradation on the SHM system reliability. This paper aims to formulate a general framework for evaluating SHM reliability that takes sensor failures into account. The framework involves modelling sensor network degradation processes using Petri nets (PNs) and calculating the expected information gain of the sensor network. The PNs allow for identifying the location and number of sensor failures. Kullback–Leibler (KL) divergence with Bayesian inversion is used to calculate the expected information loss due to sensor failure. Two case studies are used to illustrate the methodology: (i) a damage localization scheme using an ellipse-based time-of-flight (ToF) model and (ii) a damage identification scheme using a guided waves damage interaction model. The proposed framework is demonstrated by both numerical and physical experimental case studies. Whereas the case studies are specific to an ultrasonic guided wave monitoring system, the proposed approach is generic. The proposed model is able to predict the health condition state and utility of SHM, which can potentially help in constructing asset management models in various industries.

1. Introduction

SHM plays a vital role in ensuring the integrity of engineering infrastructure. Its primary objective is the implementation of a systematic approach to detect and identify potential damage or structural issues within these critical assets [1]. As those responsible for public safety and the extended functionality of infrastructure, engineers and infrastructure managers rely on SHM systems to provide real-time or periodic assessments, enabling timely maintenance and preventive measures. However, the effectiveness of SHM systems is subject to the dynamic nature of the environment in which they operate. Environmental factors, such as temperature fluctuations, humidity variations, seismic activity, and other external forces, can significantly impact the performance of SHM equipment [2,3]. These changes can affect the accuracy and reliability of data collected, potentially leading to false alarms or missed issues. Furthermore, the aging process poses an inherent challenge to SHM systems. Over time, the components of these systems can undergo wear and tear, resulting in reduced functionality and sensitivity [4]. This degradation may compromise the system's ability to provide accurate and timely assessments, diminishing its overall utility. Therefore, there is an important need to quantify the reliability of SHM systems considering sensor failures.

Reliability analysis in SHM focuses on developing methods to evaluate the reliability of these three aspects: damage detection, damage localization, and damage identification. These evaluations are typically defined in terms of specific metrics [5]: (1) Probability of detection (PoD): This metric assesses the likelihood that the SHM system correctly detects the presence of damage. It is crucial in determining how dependable the system is in recognizing structural issues. (2) Probability of localization: This metric evaluates the accuracy of the SHM system in localizing the detected damage. It demonstrates the system's ability to locate the location of structural defects. (3) Probability of sizing: This metric is related to the system's capacity to accurately estimate the size, extent, or severity of the damage. It is particularly important in assessing the significance of the structural issue.

* Corresponding author.
E-mail address: wen.wu1@nottingham.ac.uk (W. Wu).

https://doi.org/10.1016/j.ress.2024.110267
Received 5 December 2023; Received in revised form 30 May 2024; Accepted 7 June 2024
Available online 10 June 2024

Researchers have often borrowed traditional methods from non-destructive testing (NDT) as a foundational basis for developing SHM reliability evaluation techniques, such as the probability of detection curve [5]. Gianneo et al. [6] extended a multi-parameter PoD approach from NDT to a guided waves-based SHM system. Additionally, Tschöke et al. [7] extended the Berens model to guided wave-based SHM systems, employing a computer-aided approach that substantially lowered experimental costs. However, it is not enough to rely solely on conventional NDT PoD curves in the context of SHM. Firstly, SHM involves more sources of variability compared to NDT, such as sensor degradation as sensors in SHM are permanently installed, making it challenging to capture all these sources accurately [8,9]. Secondly, conventional PoD curves typically assume zero uncertainty in the size of detected damage, which does not always align with real-world conditions of SHM applications [5].

Recently, considerable efforts have been made to assess the performance of monitoring systems. Zhang et al. [10] employed a stochastic degradation model and Bayesian theorem to simulate the dynamic performance of monitoring systems, including PoD and probability of false indication. These metrics were quantitatively analysed through Value of Information (VoI) analysis. To assess the contributions of CM from a cost-efficiency standpoint, the research introduced an analytical framework for the Value of CM Information Analysis, which integrates condition-based maintenance actions into Risk-Based Inspection (RBI) planning. Falcetelli et al. [11] established a systematic approach based on the Length at Detection method to qualify Distributed Optical Fibre Sensors for damage detection probability in composites under different scenarios by introducing the concept of virtual specimens. In [12], a framework based on Dynamic Bayesian Networks was introduced for quantifying the value of SHM information, factoring in measurement bias and the degradation of monitoring performance. Specifically, it presents a comprehensive model to address SHM information uncertainties, including the effects of random errors and measurement bias. Kamariotis et al. [13] developed a framework to quantify of the value of vibration based SHM, using a Bayesian filter for the tasks of sequential joint deterioration state-parameter estimation and structural reliability updating. Drawing from the analysis of existing studies, it becomes evident that the field lacks reliability metrics for defect localization and sizing. Hence, there is a clear need for further exploration and development in the field of SHM system reliability evaluation.

In information theory, KL divergence (also called relative entropy) is a measure of the distance between two distributions [14]. In the context of Bayesian updating, the prior PDF (probability density function) is the state of knowledge before any measurement data is available; the posterior PDF is the state of knowledge of the distribution of the model parameters after updating the prior information with the measurement data. KL divergence has been used to optimize the sensor placement of SHM systems, based on which a concept called information gain (IG) is proposed [15,16]. In [15], the expected IG was presented for optimally designing the locations of strain sensors in a structure for the purpose of identifying cracks using strain measurements. In [16–18], a systematic approach is proposed for optimizing the layout of ultrasonic guided wave transducers in different forms of structures by combining the information value with IG and sensor costs. In general, IG can be used to evaluate the potential value of a sensor network and further indicate the performance of an SHM system.

In the realm of SHM, there have been a limited number of models developed to simulate the impact of sensor degradation on the SHM reliability comprehensively. In [19], degrading engineering systems monitored by degrading sensors is considered. In particular, Wiener process is used to model degradation of the sensor with increasing measurement error. Maximum likelihood estimation is used to estimate the parameters associated with the sensor degradation process. PNs are graphical and mathematical modelling tools that can be used not only for visual communication but also for building state equations and algebraic equations [20]. They have been used to model and manage risk in a wide range of fields [21,22]. Many researchers also use PN for failure process simulation. Andrews et al. [23] proposed a degradation model for railway track based on the PN method, which can produce distributions of times for the track geometry to degrade to a specified state. Le and Saleh [24,25] have applied PNs to simulate the degradation process of wind turbines. Due to their flexibility and their capability when simulating dynamic processes, PNs are adopted here to simulate the degradation process of sensors.

The current study presents a novel methodology for evaluating the reliability of SHM systems in the context of sensor failures. It involves a multi-step approach, starting with a PN module that simulates sensor network degradation, yielding data on the number and locations of failed sensors. Subsequently, a mathematical formulation for calculating IG for each failed sensor layout is provided, which quantifies the value of information when a sensor has failed. Two case studies are proposed to validate the methodology. In the first, finite element models are employed to localize damage via Bayesian inference, integrating ToF features and an analytical model. A second case study based on a physical ultrasonic guided wave experiment is conducted for damage size identification, incorporating scattering coefficients and a semi-analytical method with Bayesian inference. Next, the study establishes a relationship between SHM system performance indicators and IG. By integrating these modules, the methodology assesses the monitoring performance of the SHM system, encompassing accuracy and uncertainties over its operational lifetime. This approach provides a single value to evaluate the reliability of SHM systems, accounting for sensor failures under various performance aspects. The methodology has been successfully applied in both numerical and physical experimental case studies, demonstrating the ability of the proposed approach to track monitoring performance over sensor failure.

In summary, the paper introduces three innovative aspects:

- Firstly, it outlines a flexible failure model that can be readily expanded and can accommodate diverse types of failure history data, including time-series failure data and failure rates. This model is designed to simulate the degradation process in various sensor networks effectively.
- Secondly, it introduces a method for calculating information gain, aimed at evaluating the contribution of each sensor within the network, considering measured and modelled uncertainties.
- Finally, it proposes a framework for assessing the probability of localization and sizing within a SHM system, taking into account the potential for sensor failure.

The manuscript is organized as follows. Section 2.1 introduces the basic PN concepts and the PN module to simulate sensor degradation. Section 2.2 shows the mathematical formulation of IG calculation. Section 2.3 provides an outline of the proposed methodology. Sections 3 and 4 introduce both a numerical and a physical application of damage localization and identification, which shows detailed step-by-step insights into the calculation and verification processes. An illustrative example of the overall methodology integrating PN and IG is provided in Section 5. Finally, conclusions are included in Section 6.

2. Methodology

There are two main tasks that need to be handled when evaluating the reliability of SHM. First, it is necessary to describe the failure process of sensors. Second, the effect of sensor failure on the utility of SHM must be evaluated.

2.1. Stochastic degradation modelling of sensor networks by PN

2.1.1. Basic Petri net concepts

Due to their flexibility and applicability to dynamic process simulation, Petri net models are used to build an degradation model for sensor failure [26]. PNs consist of four elements: places, transitions, arcs, and

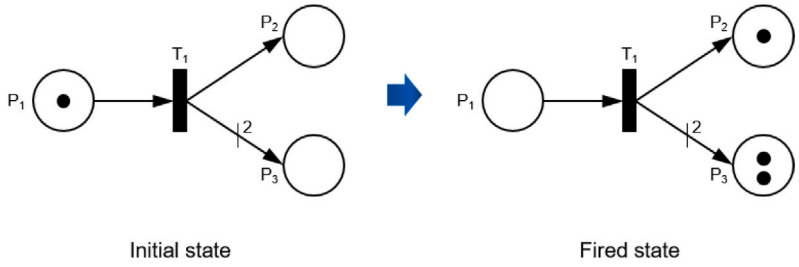

Fig. 1. A simple PN model before and after transition firing.

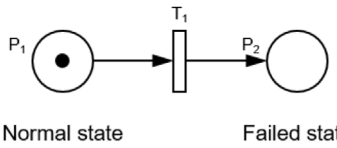

Fig. 2. PN describing the degradation process of each sensor.

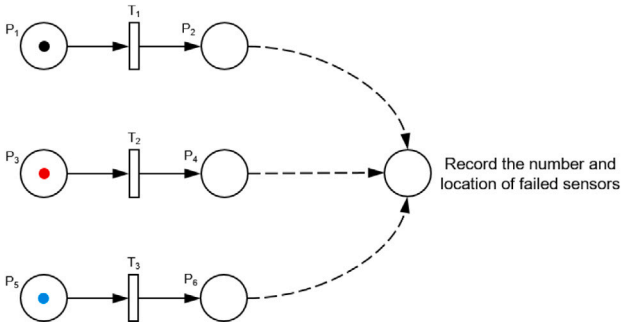

Fig. 3. PN describing the degradation of a sensor network.

tokens [26]. The PN is described by circular nodes, called places, and rectangular nodes, called transitions, with a number of directed arcs connecting places and transitions. The state of a PN is described by its marking, which is defined according to the distribution of tokens in the places. Tokens are moved from, or added to places based on firing rules. A transition is enabled if all of its input places are marked with a required number of tokens defined by the weight of the corresponding connecting arcs. The transition can fire immediately or after a specified delay. Firing removes an arc weight amount of tokens from each input place and adds an arc weight amount to each output place [20,27].

To aid understanding, a simple example is given in Fig. 1. The left side of a PN is the initial state. In this paper, place 1 will be referred to as P_1, transition 1 as T_1 and so on. In this PN, T_1 has one input place, P_1, and two output places, P_2 and P_3. Since P_1 is initially marked, the transition is enabled and after a delay, it will fire. During firing, one token is removed from P_1 and one/two tokens added to P_2 and P_3 respectively, due to the weight of the arcs connecting each of them to T_1. The state of the PN after firing is shown on the right side.

2.1.2. Sensor degradation process description

The degradation process of a sensor is defined by two states: normal state and failed state, as shown in Fig. 2. In the normal state, the sensor functions correctly, while the failed state indicates that the sensor has malfunctioned and cannot receive signals. Places represent different degradation states, and transitions govern the transition times between different states. The transition follows a Weibull distribution with scale parameter η and shape parameter β. P_1 and P_2 represent the normal and failed states, respectively. The Weibull parameters can be estimated using historical sensor failure data. For estimating, both manual and computational approaches can be employed [27].

The sensor network of an SHM system is composed of numerous sensors. Failures of various sensors in various places lead to differing effects on the monitoring accuracy of the SHM system. Thus, each sensor failure must be considered separately. The PN modelling a sensor network's failure process is shown in Fig. 3, using 3 sensors as an illustrative example. It is assumed that each sensor will fail independently and in accordance with the same degradation pattern. P_1, P_3 and P_5 stand for the normal state. P_2, P_4 and P_6 stand for the failure state. T_1, T_2 and T_3 follow the Weibull distribution. The failure sensor number and location are recorded based on the token numbers in places from P_1 to P_6.

To minimize complexity, the case where the sensor network is either working or failed is selected. It is true that different kinds of sensor failures occur and have varying effects on the signal. However, the impact on the signal relates to the degree of errors caused by different failure mechanisms. Consequently, the proposed methodology is still applicable to different failure states as long as the signal error resulting from sensor failure can be measured. Another reason for this assumption is the absence of detailed sensor failure data, including temporal failure patterns. With access to such data, extending the Petri net model to simulate various failure states would be a desirable avenue for future work.

2.2. Information gain evaluation of failed sensors

Within the SHM system, each sensor is capable of generating a variety of data, including ultrasonic signals, vibration signals, and acoustic signals. Engineers apply different techniques to interpret these signals, aiming to extract crucial information about the structural condition, such as identifying defect locations and assessing defect sizes. However, it is crucial to acknowledge that not all sensor data are of equal importance; some sensor data carry more significance than others. Moreover, signal errors originating from each sensor also play a role in determining its IG value. By clearly understanding the value of each sensor, the potential impact of sensor failure (a sensor can no longer provide data) on our ability to assess the condition of a structure can be predicted.

KL divergence is used as a scalar measure of the IG about a random variable θ between the prior and posterior PDFs [14,28]. The available sensor data $\mathcal{D}$ from the SHM system will vary as the sensor configuration alters. The IG for various sensor configurations will then be reflected in the KL divergence. Therefore, it is ideal to evaluate the IG value of sensors based on the change of KL divergence. The definition of IG for each sensor layout, based on the KL divergence, is presented below:

$$\begin{aligned}\mathrm{IG}(\mathcal{D},\mathbf{C^n}) &= \mathrm{KL}(p(\theta \mid \mathcal{D},\mathbf{C^n}) \parallel p(\theta,\mathbf{C^n})) \\ &= \int \log_2\left[\frac{p(\theta \mid \mathcal{D},\mathbf{C^n})}{p(\theta,\mathbf{C^n})}\right] p\left(\theta \mid \mathcal{D},\mathbf{C^n}\right) d\theta\end{aligned} \tag{1}$$

where $p(\theta,\mathbf{C^n})$ denotes the prior PDF of the parameters θ; $p(\theta \mid \mathcal{D},\mathbf{C^n})$ represents the posterior distribution of θ with the available signal; and $\mathbf{C^n}$ denotes the sensor configuration, including the number and position

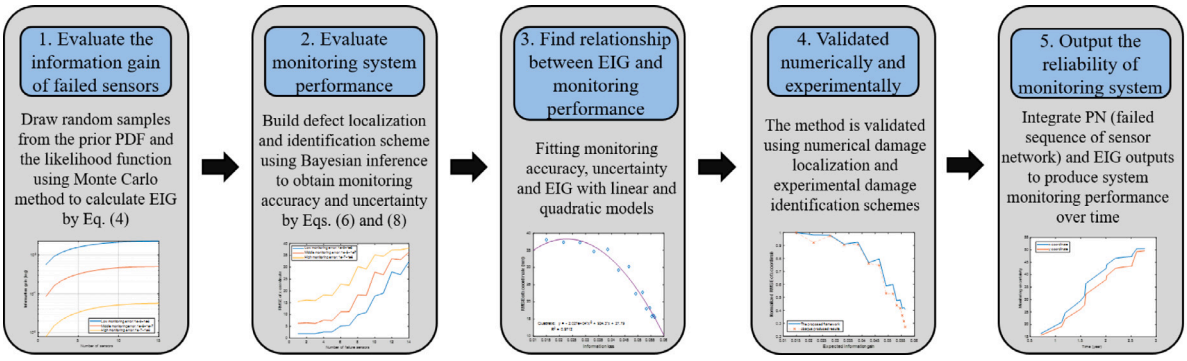

Fig. 4. Workflow of the proposed framework.

of sensors. Note that the IG equals zero if the posterior distribution is the prior distribution.

During this design stage of the SHM system, where real damage information is unspecified, the reliability of the system must consider all potential scenarios, leading to the calculation of the expected information gain (EIG) through a pre-posterior analysis:

$$\mathrm{EIG}(\mathcal{D}, \mathbf{C^n}) = \int_{\mathfrak{D}} [\mathrm{KL}(p(\boldsymbol{\theta} \mid \mathcal{D}) \parallel p(\boldsymbol{\theta}))]\, p(\mathcal{D}) d\mathcal{D} \tag{2}$$

The signals obtained from sensors carry varying levels of experimental error, which can affect the IG. To account for these errors, the EIG can be reformulated as follows:

$$\mathrm{EIG}(\mathcal{D}, \mathbf{C^n}, \boldsymbol{\xi}) = \int_{\boldsymbol{\xi}} \int_{\mathcal{D}} [\mathrm{KL}(p(\boldsymbol{\theta} \mid \mathcal{D}) \parallel p(\boldsymbol{\theta}))]\, p(\mathcal{D}) p(\boldsymbol{\xi}) d\mathcal{D} d\boldsymbol{\xi} \tag{3}$$

where $\boldsymbol{\xi}$ represents a sensor's experimental error. The above equation has a double multidimensional integral problem, which can be solved numerically using the Monte Carlo method, as demonstrated below [15,16]:

$$\mathrm{EIG} \approx \frac{1}{N_{\boldsymbol{\xi}}} \sum_{z=1}^{N_{\boldsymbol{\xi}}} \left[\frac{1}{N_{\mathrm{out}}} \sum_{m=1}^{N_{\mathrm{out}}} \left[\log_2 p\left(\mathcal{D}_{(m)} \mid \boldsymbol{\theta}_{(m)}, \boldsymbol{\xi}_{(z)}\right) - \log_2 \left(\frac{1}{N_{\mathrm{in}}} \sum_{k=1}^{N_{\mathrm{in}}} p\left(\mathcal{D}_{(m)} \mid \boldsymbol{\theta}_{(k)}, \boldsymbol{\xi}_{(z)}\right) \right) \right] \right] \tag{4}$$

where $N_{\boldsymbol{\xi}}$ represents the number evenly sampled from the range of $\boldsymbol{\xi}$; $\boldsymbol{\theta}_{(m)}$ is a sample from the prior distribution $p(\boldsymbol{\theta})$; N_{out} denotes the number sampled from the prior distribution; $\mathcal{D}_{(m)}$ is a sample from the likelihood distribution $p(\mathcal{D}_{(m)} \mid \boldsymbol{\theta} = \boldsymbol{\theta}_{(m)})$; and N_{in} denotes the number sampled from the likelihood distribution.

The EIG of each sensor configuration can be evaluated by Eq. (4). The accuracy and uncertainty of SHM monitoring is a direct indication of the SHM reliability. There is no clear mathematical relationship between EIG and the accuracy and uncertainty of SHM monitoring. To define reliability using EIG, the relationship between EIG and the accuracy and uncertainty of SHM monitoring must be established.

2.3. Outline of the proposed methodology

The proposed methodology in this study integrates PNs and Bayesian inversion algorithms. The summarized steps of the evaluation method are shown in Fig. 4. There are five steps in the framework: EIG evaluation of failed sensors, monitoring system performance evaluation, finding the relationship between EIG and monitoring performance, numerical and experimental verification, and output of monitoring system reliability. In the following sections, each step is described in detail.

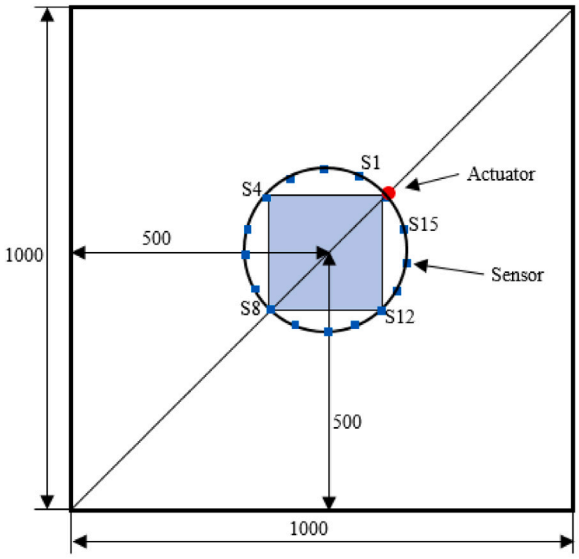

Fig. 5. Plate geometry and sensor layout.

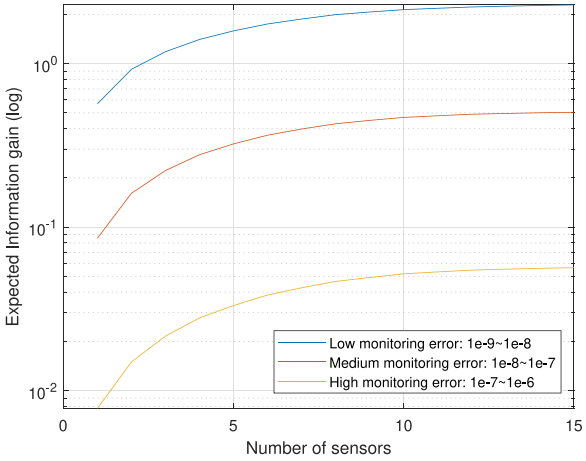

Fig. 6. Information gain with increasing number of sensors under different uncertainties.

3. Application on guided wave based damage localization

The proposed methodology is illustrated using a case study about damage localization with guided waves using ToF model based on Bayesian inverse approach in a metallic plate. The dimension of the

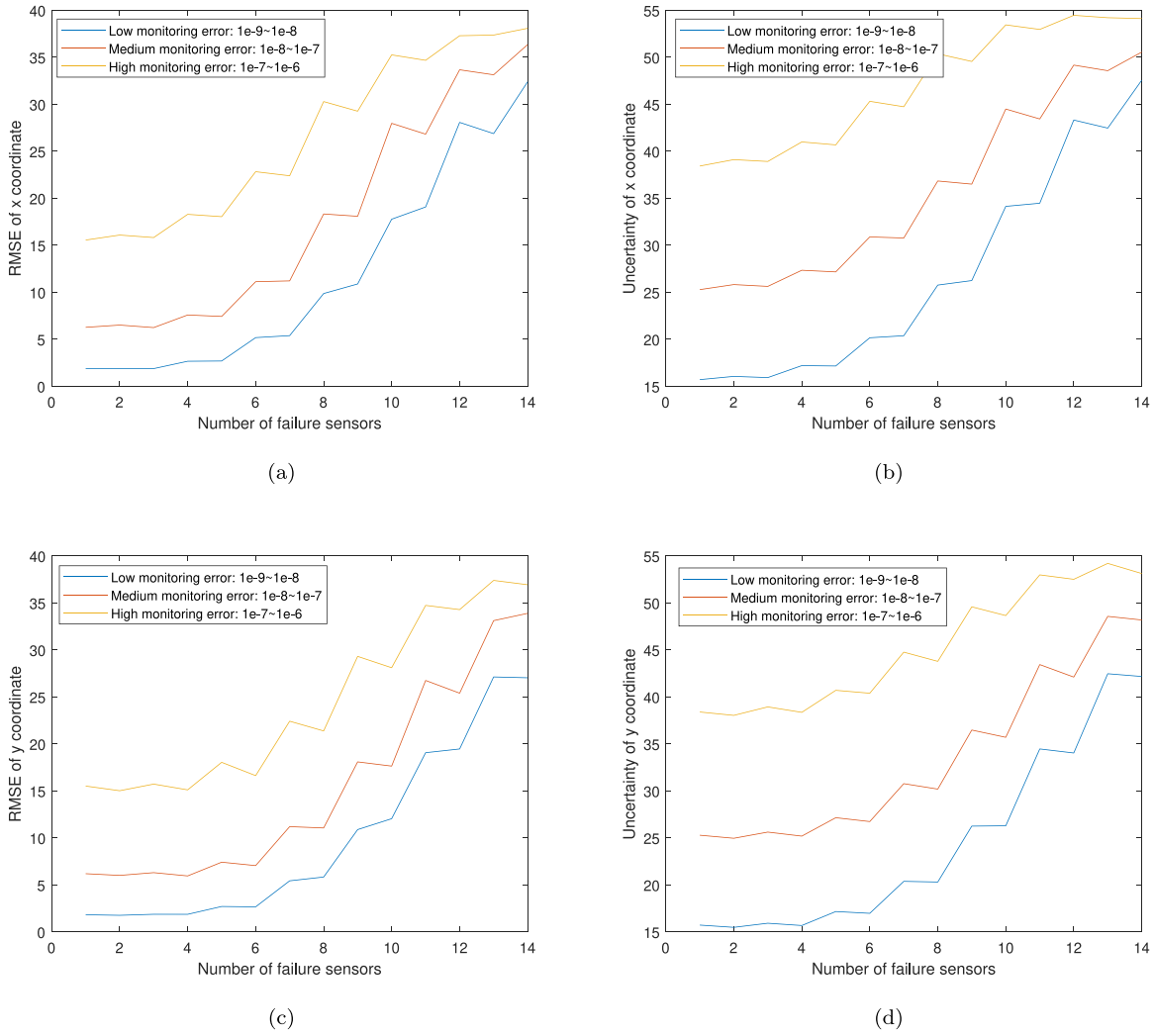

Fig. 7. (a) RMSE of x coordinate, (b) uncertainty of x coordinate, (c) RMSE of y coordinate and (d) uncertainty of y coordinate produced by Bayesian inference.

specimen is $L_x = 1000$ mm, $L_y = 1000$ mm in size and 2 mm in thickness. The material properties for steel are as follows: elastic modulus $E = 210$ GPa, density $\rho = 8100$ kg/m^3 and Poisson ratio $\nu = 0.3$. The configuration of different piezoelectric (PZT) sensors and a plate with geometry information are shown in Fig. 5. The actuator represented by a red dot has been used to generate a sinusoidal burst, and the PZT sensors received signals. In order to be consistent with the sensor layout of the experimental damage identification case study (Fig. 10), the damage localization case study also uses a circular sensor layout. PZT sensors are mounted on the structure's surface radially with equal spacing. The square light blue area with a side of length 200 mm is the area where defects may appear.

3.1. Step 1: Information gain calculation

Section 2.2 presented an EIG function with the failure of the sensor network, which requires updated information about the model parameters for each candidate damage location. In this section, the updating of likelihood function for damage localization using Bayesian inference is presented. The problem of damage localization is addressed by a model-based Bayesian inference using an ellipse-based ToF model [16,29]. The time difference between the incident and damaged-scattered waves is known as the difference in ToFs. This can be determined using coordinates of the damage position, the sensor and the actuator, as well as the wave propagation speed in an ellipse-based model [29,30]. This analytical model is used to construct the likelihood function.

The unknown model parameters are considered to be the coordinates of damage, denoted as $\boldsymbol{\theta}_L$. The measured and the modelled ToF are different because of epistemic and aleatoric uncertainty. The prediction error equation can be used to continue with the Bayesian formulation for parameters estimation, as follows:

$$\mathrm{ToF}_D^{(a-s)} = \mathrm{ToF}_M^{(a-s)}(\boldsymbol{\theta}_L) + \mathbf{e_L} \tag{5}$$

where $\mathrm{ToF}_D^{(a-s)}$ and $\mathrm{ToF}_M^{(a-s)}(\boldsymbol{\theta}_L)$ represent experimental and modelled ToF, respectively. A zero mean Gaussian distribution with covariance matrix $\Sigma_e = \mathrm{diag}(\sigma_{e,1}^2, \sigma_{e,1}^2, \ldots, \sigma_{e,N_L}^2)$ is selected to model the error term $\mathbf{e_L}$ in order to produce the largest prediction uncertainty, i.e., $\mathbf{e} \sim \mathcal{N}(0, \Sigma_{e_L})$. This is based on the principle of Maximum Information Entropy [31,32]. Nevertheless, the impact of bias on information modelling has been explored in [33,34]. The value of information is influenced not only by random measurement errors but also by bias (systematic errors), making it an important consideration for future research. Based on this assumption, the formula of a likelihood function is shown below:

$$\begin{aligned} p\left(\mathrm{ToF}_D^{(a-s)} \mid \mathrm{ToF}_M^{(a-s)}, \boldsymbol{\theta}_L, C^n\right) = & \frac{1}{(\sqrt{2\pi})^n \sqrt{\det \boldsymbol{\Sigma}(\boldsymbol{\sigma})}} \exp\left(-\frac{1}{2}\left[\mathrm{ToF}_M^{(a-s)}\right.\right. \\ & \times \left(\boldsymbol{\theta}_L, C^n\right) - \mathrm{ToF}_D^{(a-s)}(C^n)\Big]^T \\ & \boldsymbol{\Sigma}(\boldsymbol{\sigma})^{-1}\left[\mathrm{ToF}_M^{(a-s)}\left(\boldsymbol{\theta}_L, C^n\right)\right. \\ & \left.\left. - \mathrm{ToF}_D^{(a-s)}\left(C^n\right)\right]\right) \end{aligned} \tag{6}$$

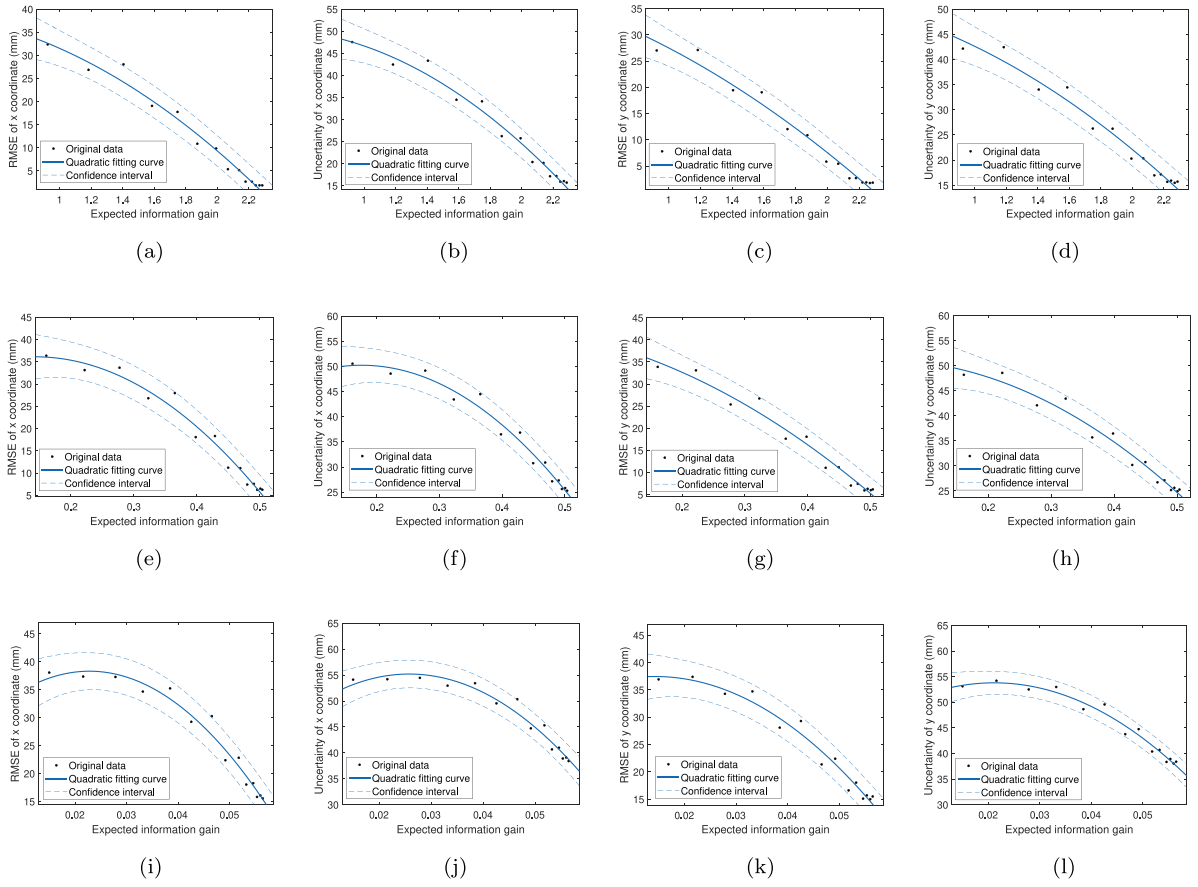

Fig. 8. Fitting relationship between EIG and (a) RMSE of x coordinate, (b) uncertainty of x coordinate, (c) RMSE of y coordinate and (d) uncertainty of y coordinate at low uncertainty level, (e) RMSE of x coordinate, (f) uncertainty of x coordinate, (g) RMSE of y coordinate and (h) uncertainty of y coordinate at medium uncertainty level, (i) RMSE of x coordinate, (j) uncertainty of x coordinate, (k) RMSE of y coordinate and (l) uncertainty of y coordinate at high uncertainty level.

The likelihood function is used in Eq. (4) to obtain the EIG of each sensor layout.

Based on the EIG calculation method, N_ξ, N_{out} and N_{in} are specified as 100, 100 and 100 respectively. The coordinate system is established with its origin at the centre of the plate, utilizing the horizontal x-axis and vertical y-axis. The prior defect locations are bounded within minimum coordinates of −50 mm and maximum coordinates of 50 mm along both axes. In Eq. (4), the variable ξ represents the nuance, non-updated quantity, which has a substantial impact on the EIG. In this case, ξ is considered as the experimental error σ. To account for this, three different uncertainty ranges are considered in our calculations: [1e−9, 1e−8] (low uncertainty), [1e−8, 1e−7] (medium uncertainty), and [1e−7, 1e−6] (high uncertainty). The EIG with increasing number of sensors under different uncertainty levels is shown in Fig. 6. The number of sensors ranges from 1 to 15. Each sensor combination shown in Fig. 6 represents the optimal layout for the current number of sensors. For instance, when there is only 1 sensor, the figure displays the optimal value in the optimal position for that single sensor, and so on. The observation reveals that as the number of sensors increases, the EIG steadily rises until it reaches a stable level. Notably, the EIG reaches the steady level earlier at lower uncertainty levels compared to higher uncertainty levels. This indicates that in scenarios with high levels of uncertainty, which equate to high levels of error, a greater number of sensor signals are required to reach the steady level of EIG. Additionally, it is seen that the EIG value is higher under low uncertainty compared to high uncertainty. This suggests that accurate signals provide us with more information.

3.2. Step 2: Monitoring accuracy and uncertainty evaluation

Using Bayes' theorem, the ToF model and likelihood function explained in Section 3.1, employing various signal inputs for inversion, allows us to determine the two coordinate parameters of the defect location. For more detailed information on the inversion process, refer to [29]. Uniform prior distributions are used with bounds [−50, 50] mm for coordinate x and [−50, 50] mm for coordinate y. The non-updatable standard deviation σ is changing based on the assorted signal uncertainty level. Samples from the posterior PDFs of each set of model parameters are obtained through Metropolis–Hastings (M–H) algorithm [35,36] using 50 000 samples and a Gaussian proposal distribution with appropriate standard deviation to ensure acceptance rate within the interval [0.2, 0.4] [37–39].

To obtain accurate and representative defect coordinate error and uncertainty values, numerous calculations involving varying uncertainties and defect locations are performed. The final values were determined by averaging the results across these calculations. Different potential damage locations are selected in a 5 × 5 grid with spacing 25 mm included in the blue square shown in Fig. 5. In each Bayesian inference calculation, a constant standard deviation value is chosen. So, for each uncertainty level defined in the information gain calculation, four evenly-distributed different standard deviation values are chosen. These values aimed to account for model and experimental uncertainties, such as signal errors and analytical model inaccuracies.

The signals recorded by various sensors served as the input data for Bayesian inference. The signals are generated by FEM, details will be given in Section 3.4. If a sensor fails, the corresponding signal will

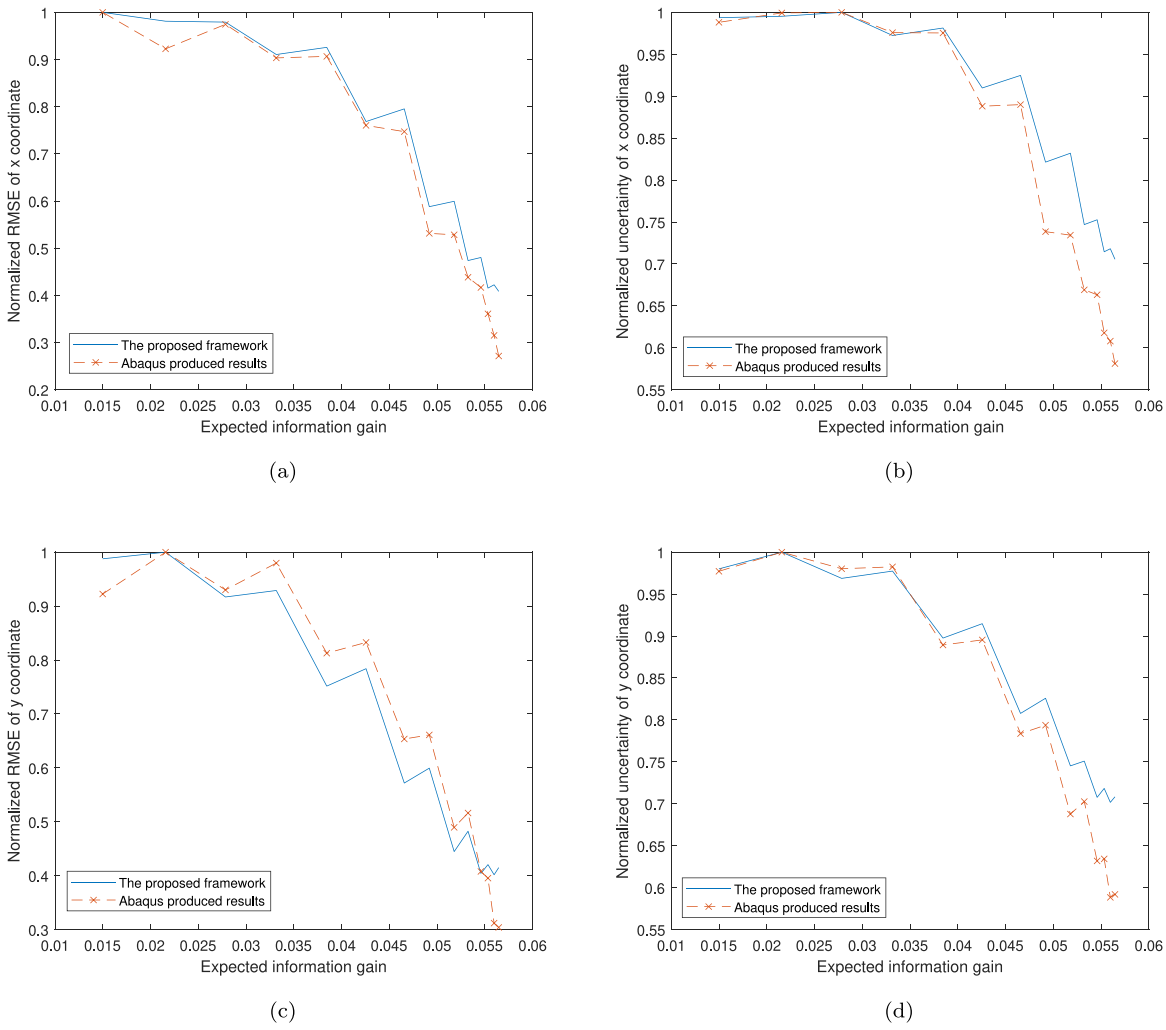

Fig. 9. Validation of the relationship of EIG with (a) RMSE of x coordinate, (b) uncertainty of x coordinate, (c) RMSE of y coordinate and (d) uncertainty of y coordinate verified by Abaqus.

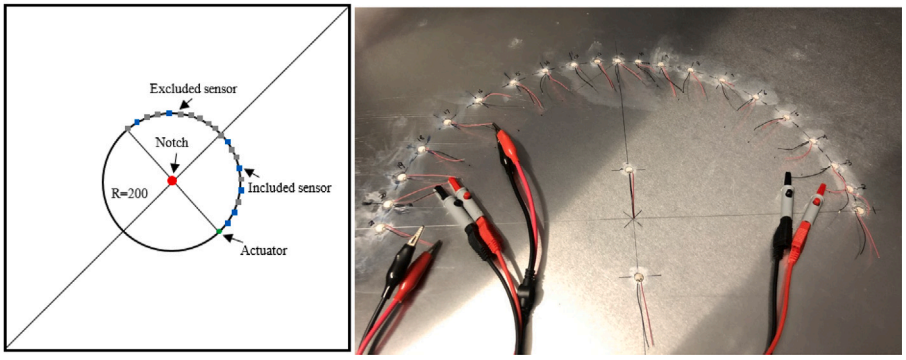

Fig. 10. Sensor layout in a physical experiment.

be removed from the available data. In the context of the sensor layout shown in Fig. 5, for a total of 15 sensors, factorial of 15 possible number of sensor failures existed, which presents a significant computational challenge. In this situation, to reduce computational complexity, the simplifying assumption is made that the failure of each sensor was the most sensitive in the current sensor layout. If only one sensor fails at a time, the sensor that fails each time is the most sensitive sensor, resulting in 15 possible failure scenarios. Usually 3 pair of sensors are required by using ToF triangulation approach to localize damage. However, within Bayesian inference, a prior information can be assumed to tackle the non-uniqueness inherent in the inversions [40,41]. Specifically, uniform intervals of potential damage locations have been given when doing inference, which makes it possible to obtain damage locations under non-uniqueness situations. Therefore, a minimum of two signals are necessary to infer the damage location. Thus, the worst-case scenario entails two sensors remaining operational, reducing the

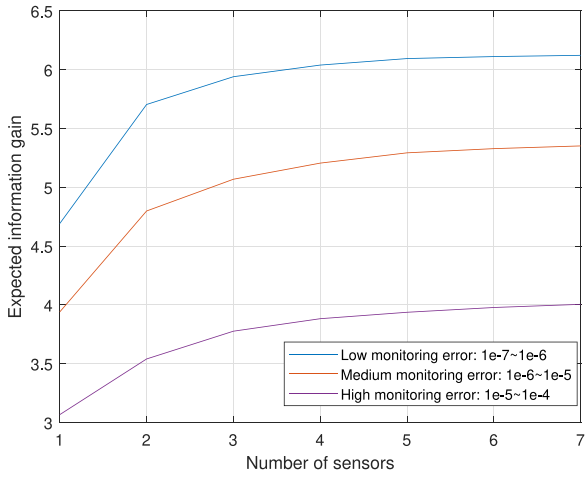

Fig. 11. Information gain with the increase of sensor numbers under different uncertainties.

combinations to 14. The available ToF for each sensor was generated using the analytical model, introducing a certain level of Gaussian noise.

Monitoring accuracy is quantified by computing the root mean square error (RMSE) between the value of the true damage location and the mean value of posterior distributions of inferred damage locations. On the other hand, monitoring uncertainty is assessed by calculating the standard deviation of the posterior distribution of inferred damage locations.

The resulting RMSE and uncertainty in the x and y coordinates of damage locations are detailed in Fig. 7. It is seen that as the number of failed sensors increases under different uncertainty levels, both the RMSE and uncertainty gradually increase. This implies that as less information is available due to sensor failures, the RMSE and uncertainty grow. Additionally, the RMSE and uncertainty are smaller for lower levels of uncertainty compared to higher levels of uncertainty, indicating that higher sensor error levels lead to lower information value. It is observed that sometimes the RMSE becomes small as number of failure sensors increases. This phenomenon can be attributed to two primary factors. First, the calculation of RMSE and uncertainty depends on averaging the outcomes from various chosen potential damage locations. Expanding the number of these selected locations tends to smooth out the curve, however, this also leads to increased computational effort. Second, the determination of RMSE and uncertainty employs a probabilistic Bayesian inference model. As the pool of available signal sources diminishes (more failed sensors), the accuracy of the inference declines. This explains why the curve appears smooth when the count of failed sensors is low, but becomes more jagged, resembling a sawtooth pattern, as the number of failed sensors rises.

3.3. Step 3: Relationship between information gain and monitoring accuracy and uncertainty evaluation

As mentioned earlier, monitoring accuracy and uncertainty are direct indicators of the reliability of the monitoring system. To use EIG to represent monitoring system reliability, it is essential to establish the relationship between EIG and monitoring accuracy and uncertainty. This relationship is depicted in Fig. 8 at different uncertainty levels, and a quadratic model fitted. For instance, in Fig. 8(a) and (b), it is observed that the inferred RMSE and uncertainty on the x-coordinate exhibit a nearly quadratic relationship with EIG. The 90% confidence interval of the fitting relationship is provided as well. It is observed that the fitting results are reasonable.

3.4. Step 4: Numerical validation

In order to verify the relationship, a numerical case study is provided. FEM commercial software Abaqus is used to simulate guided waves, which can be used to excite and receive signals numerically [42]. The geometry and material properties provided in Fig. 5 are used. A 2 mm radius circular hole is modelled at the centre of the plate. An incident plane wave of fundamental S0 mode is generated by applying a transient displacement at the actuator location. The forcing function is a 4 cycle Hanning windowed sinusoid with a central frequency of 100 kHz and a time duration of 40 μs. The model is meshed by using 8-node general purpose linear brick elements (C3D8R), with reduced integration and maximum element edge length of 1.8 mm [42]. The total number of elements is 671,474. A circular monitoring contour at which the displacement components are observed is specified in the vicinity of the damage. The signals are received at 15 nodes in the monitoring contour. The simulations are performed separately for pristine and damaged states, and the signals obtained are subtracted to obtain scattered waves. Finally, the scattered waves are localized to obtain ToF.

Following the Bayesian inference procedure proposed in [29,43], the damage's location with different sensors can be inferred. The uncertainty level is determined by the standard deviation of the error in the Abaqus-simulated ToFs when compared with the ellipse-based model. Based on the uncertainty level of Abaqus-simulated ToFs, it is located in the higher uncertainty level [1e−7, 1e−6]. Therefore, Abaqus results with the above curves calculated using the highest level of uncertainty are compared. Note that all the values are normalized by their maximum value. The results are shown in Fig. 9. It is observed that they match well, which provides a proof of the effectiveness of the proposed framework.

4. Application on guided wave based damage identification

In this Section, an experimental case study of an aluminium plate with a part-depth circular hole based on guided waves using a semi-analytical wave damage interaction model is presented to validate the proposed framework. The experiment and damage identification methodology were published in [43].

The plate has dimensions $L_x = 1000$ mm, $L_y = 1000$ mm and a depth of 0.9 mm with elastic modulus $E = 69$ GPa, density $\rho = 2705$ kg/m^3 and Poisson ratio $\nu = 0.33$. The defect is located in the centre of the plate. The prior radius and depth ranges of a part-depth circular hole defect are [1.5 mm, 4.5 mm] and [0.1 mm, 0.4 mm], respectively. The configuration of different PZT sensors is shown in Fig. 10. The green PZT has been used to generate a sinusoidal burst, and the rest of the PZT sensors received the reflected and scattered signals. PZT sensors are mounted on the structure's surface radially with equal spacing. Based on the results presented in the previous work [43], only seven sensors were included within the damage identification scheme. To be consistent with previous work, only seven sensors are considered here, which are indicated by blue squares. The remaining sensors are represented by grey squares.

4.1. Step 1: Information gain calculation

A physics-based Bayesian inference approach utilizing a scattered field of guided waves is used to address the problem of damage identification, which was previously published by the authors in [43]. The scattered field that is dependent on the geometry of the defect is generated when a travelling wave interacts with it. Thus, the type and severity of the damage can be identified by analysing the scattered field. A semi-analytical forward model is employed to perform rapid computations on wave/damage interactions, including wave scattering, which is based on a combination of the Kirchhoff plate theory for flexural motion and the elementary Poisson theory for extensional

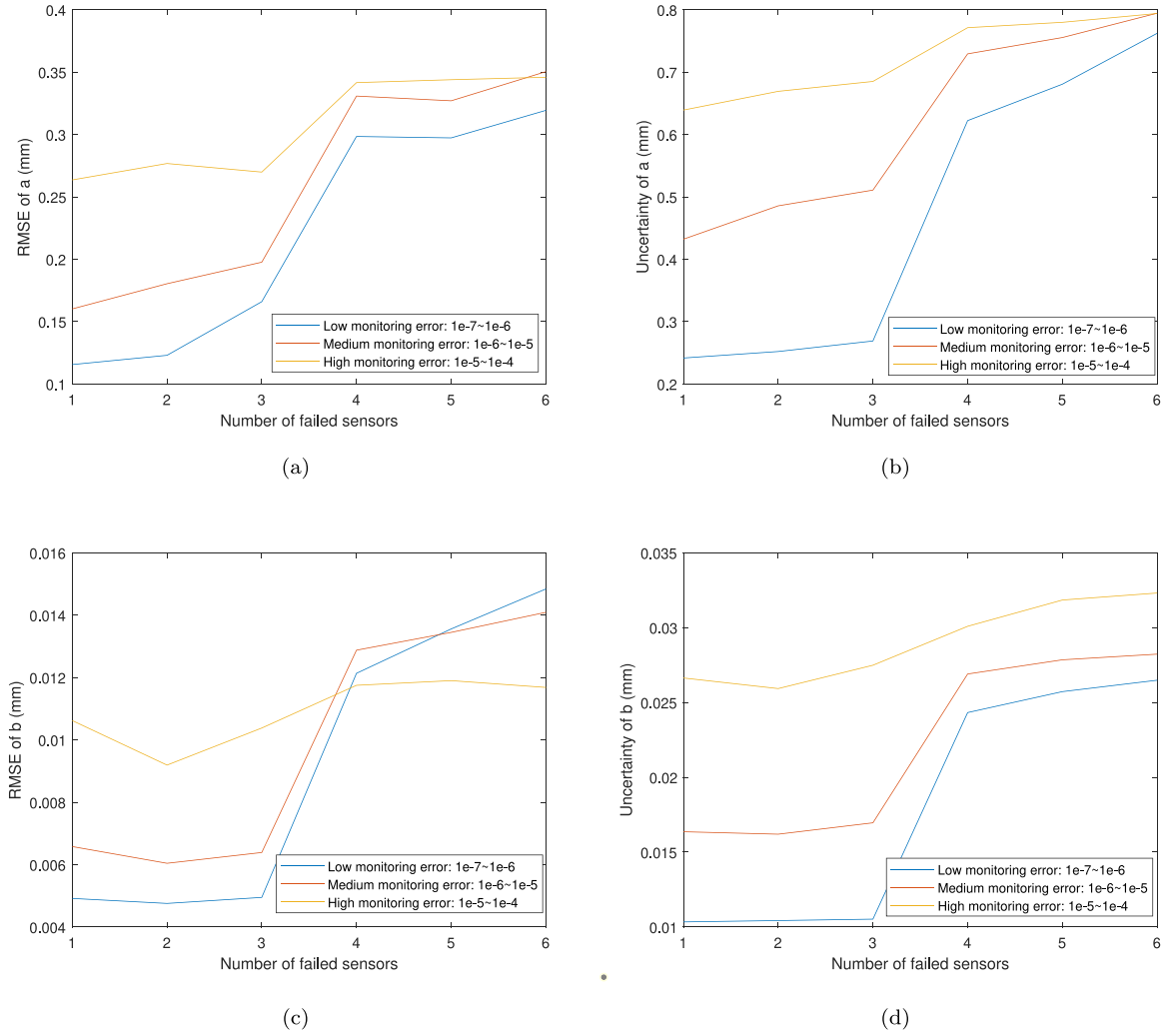

Fig. 12. (a) RMSE of a, (b) uncertainty of a, (c) RMSE of b and (d) uncertainty of b produced by Bayesian inference.

motion under the assumption of spherical problem [44]. The analytical determination of the scattering profile that is represented by $\mathbf{s}_{\mathcal{M}}(\boldsymbol{\theta}_S)$. Here, $\boldsymbol{\theta}_S$ refers to unknown model parameters, including the radius and depth of the hole. Also, there will be a difference in correctness between the measured and modelled scattering fields. The prediction error equation can be used to continue with the Bayesian formulation for parameter estimation, as follows:

$$\mathbf{s}_D = \mathbf{s}_{\mathcal{M}}(\boldsymbol{\theta}_S) + \mathbf{e}_{\mathbf{S}}. \tag{7}$$

where $\mathbf{s}_D$ represents the scattering field obtained from experiments. A zero mean Gaussian distribution with covariance matrix $\Sigma_e = \mathrm{diag}(\sigma_{e,1}^2, \sigma_{e,1}^2, \ldots, \sigma_{e,N_s}^2)$ is selected to model the error term in order to produce the largest prediction uncertainty, i.e., $\mathbf{e} \sim \mathcal{N}(0, \Sigma_e)$ [31,32]. The stochastic version of the model is given by a Gaussian distribution, as follows:

$$p\left(\mathbf{s}_D \mid \mathbf{s}_{\mathcal{M}}, \boldsymbol{\theta}_S, C^n\right) = \frac{1}{(\sqrt{2\pi})^n \sqrt{\det \boldsymbol{\Sigma}(\boldsymbol{\sigma})}} \exp\left(-\frac{1}{2}[\mathbf{s}_{\mathcal{M}}(\boldsymbol{\theta}_S, C^n) - \mathbf{s}_D(C^n)]^T \boldsymbol{\Sigma}(\boldsymbol{\sigma})^{-1} [\mathbf{s}_{\mathcal{M}}(\boldsymbol{\theta}_S, C^n) - \mathbf{s}_D(C^n)]\right) \tag{8}$$

The likelihood function is used in Eq. (4) to obtain the EIG of each sensor layout in terms of damage identification.

Based on the EIG calculation method, N_ξ, N_{out} and N_{in} are specified as 100, 100 and 10 respectively. The prior information of the defect sizes is bounded as follows: radius a [1.5, 4.5] mm and depth b [0.1, 0.4] mm. Similarly, in Eq. (4), three different uncertainty ranges: [1e−7, 1e−6] (low uncertainty), [1e−6, 1e−5] (medium uncertainty), and [1e−5, 1e−4] (high uncertainty) are introduced. The provided uncertainty values are indeed larger than those in the numerical case study (Section 3), which aligns with the expected increase in uncertainty in physical experiments. Based on the provided parameters, the EIG with the increase of sensor numbers at different uncertainty levels is shown in Fig. 11. The trend observed in the EIG values is consistent with the numerical results, showing a gradual increase followed by stabilization. Lower uncertainty corresponds to smaller EIG values, and with lower uncertainty, the values reach stability sooner.

4.2. Step 2: Monitoring accuracy and uncertainty evaluation

According to Bayes' theorem and using the scattering coefficient semi-analytical calculation method and likelihood function explained in Section 4.1, various signal inputs can be employed for inversion, allowing us to infer the defect geometry parameters. For more detailed information, refer to [43]. Uniform prior distributions are used with bounds [1.5, 4.5] mm for radius a, [0.1, 0.4] mm for depth b. The nonupdatable standard deviation σ_e with bound [1e−7,1e−4] is changing based on the signal uncertainty level. Similarly, M–H algorithm [35,36] was applied to obtain the posterior PDFs using 50 000 samples.

Based on the sensor layout provided in Fig. 10, there is a total of 7 sensors. The same assumption is made that each sensor failure

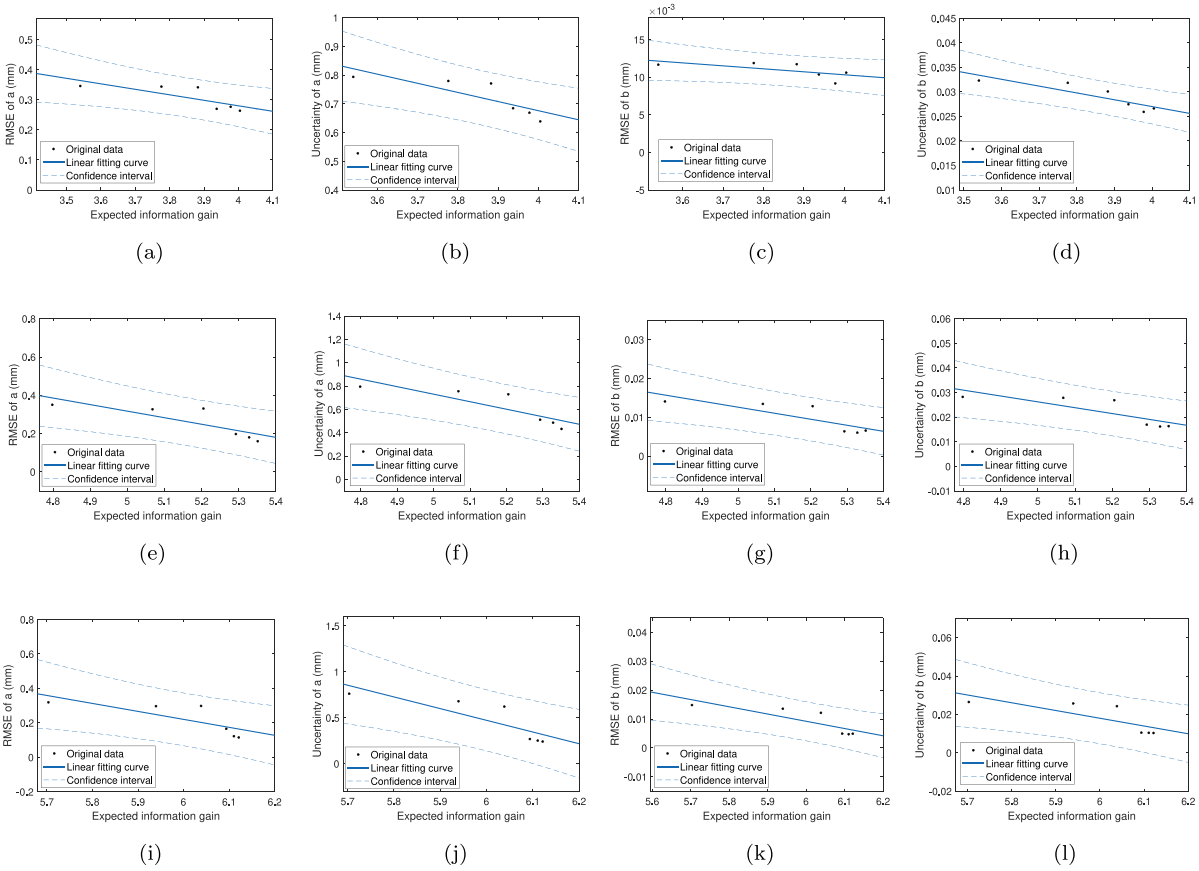

Fig. 13. Linear fitting relationship between information gain and (a) RMSE of a, (b) uncertainty of a, (c) RMSE of b and (d) uncertainty of b at low uncertainty level, (e) RMSE of a, (f) uncertainty of a, (g) RMSE of b and (h) uncertainty of b at medium uncertainty level, (i) RMSE of a, (j) uncertainty of a, (k) RMSE of b and (l) uncertainty of b at high uncertainty level.

was the most sensitive in the current sensor layout and a minimum of two sensors, resulting in 6 possible failure scenarios. Scattering coefficients at different uncertainty levels are generated using the semi-analytical model [44], introducing a certain level of Gaussian noise. Nine different potential damage sizes evenly distributed across a grid are selected. Similarly, for each uncertainty level defined in the EIG calculation, four evenly-distributed different standard deviation values were chosen. After averaging the inference results, the resulting RMSE and uncertainty of half-through thickness hole's radius and depth are shown in Fig. 12.

It is observed that, in general, an increase in the number of failed sensors leads to larger RMSE and uncertainty in the inferred defect geometry. Additionally, introducing larger uncertainties also results in greater RMSE and uncertainty in the inferred defect geometry. However, there is a slight error in the RMSE of the defect depth b. This discrepancy might be attributed to the small range of defect depth values considered in the analysis.

4.3. Step 3: Relationship between information gain and monitoring accuracy and uncertainty evaluation

To establish the relationship with 90% between monitoring accuracy, uncertainty, and EIG, this relationship is illustrated in Figs. 13 and 14 under various uncertainty levels. They are fitted using linear and quadratic models. Since there are fewer data points compared to the numerical model, the fitting results are not as precise as those of the numerical model. It is observed that the quadratic model provides a better fit compared to the linear one. However, when the EIG starts to increase within a smaller range, the RMSE and uncertainty initially increase slightly before starting to decrease. It is supposed that with the increase in EIG, the SHM system performance improves, leading to a decrease in both RMSE and uncertainty. In this case, the linear fitting is less accurate, but it provides a better representation of the overall trend. Other models might do better, but such analysis is outside the scope of this paper.

4.4. Step 4: Experimental validation

An ultrasonic experiment is used to verify the proposed methodology here. The geometry and material properties presented in Section 4 are used. In this experiment, a Keysight 33512B arbitrary waveform generator was used to generate a five-cycle sine tone-burst centred in 300 kHz, and a DSOX2014A oscilloscope was used to digitize the signals. A 3.25 mm radius half-through thickness hole is created at the centre of the plate with depth of 0.2 mm. Using frequency mode tuning and a signal processing technique presented in [43], the scattering coefficients of S0 mode from the vibration signals can be obtained.

Following the Bayesian inference procedure proposed in [29,43], the defect size with different data can be inferred. Based on the uncertainty level of experimental data, the error σ is located in the higher uncertainty level [1e−5,1e−4], which determines the uncertainty range of EIG calculation and the standard deviation of the likelihood function. The values are normalized by their maximum value. The results are shown in Fig. 15. The proposed framework and experimental results exhibit some bias but follow a similar trend. For instance, when the EIG is small, a larger RMSE prediction is generated by the proposed framework. This is primarily attributed to numerical errors occurring when the signal quality is poor, especially in cases with a high number of failed sensors. The uncertainty matches better with EIG than the RMSE. The error mainly arises from the significant uncertainty in the experimental data and the inherent errors in the analytical modelling.

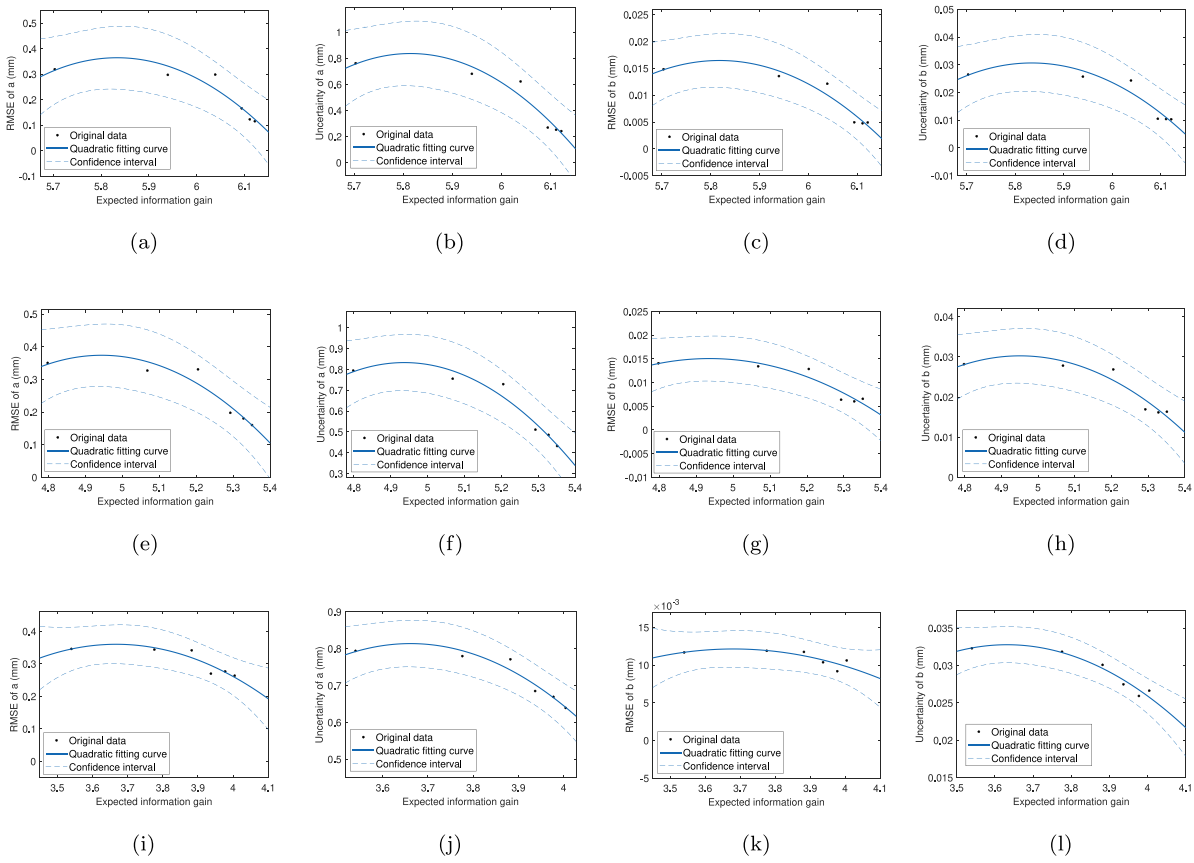

Fig. 14. Quadratic fitting relationship between information gain and (a) RMSE of a, (b) uncertainty of a, (c) RMSE of b and (d) uncertainty of b at low uncertainty level, (e) RMSE of a, (f) uncertainty of a, (g) RMSE of b and (h) uncertainty of b at medium uncertainty level, (i) RMSE of a, (j) uncertainty of a, (k) RMSE of b and (l) uncertainty of b at high uncertainty level.

5. Step 5: An illustrative example of the overall methodology integrating PN and EIG

An SHM system, once installed, serves for many years, providing crucial structural health information. It is essential to assess the reliability of the SHM system throughout its operational lifespan, not just at one moment in time. This can be achieved by integrating the PN model and EIG module in the proposed methodology.

In the initial step, the failure parameters of the sensor network are defined, and the proposed PN model is employed to simulate the degradation process of the sensor network. This PN model yields a sequence of failed sensors as its output. The relationship between EIG and monitoring performance and the sensor setup has been used to demonstrate this approach.

This is an example of how the degradation of the monitoring system is simulated by the PN, while the estimate of reliability is provided by the EIG. Given the assumption and the absence of specific sensor failure data, commonly used Weibull parameters are chosen to characterize the degradation process of all 15 sensors, with $\eta = 2.5$ and $\beta = 2.9$ [19]. The PN shown in Fig. 3 is extended to 15 sensors. After running the PN, the resulting failure sequence is as follows: [S1, S13, S2, S11, S14, S15, S5, S4, S9, S8, S6, S3, S7, S12, S10]. Next, the EIG calculation module is utilized to determine how EIG changes based on the current failure sequence at the low uncertainty level, which is shown in Fig. 16. By incorporating this with the established relationship demonstrated in Fig. 8, the changes can be derived in monitoring accuracy and uncertainty over the operational lifespan of the sensor network, which is shown in Fig. 17. The simulation results illustrate the monitoring performance of the SHM system, which can be used to support asset management decisions when the SHM system performance degrades.

The case studies provided in Sections 3 and 4 are specific to ultrasonic guided wave monitoring systems, whereas the proposed methodology for assessing reliability can be applied across various monitoring systems and real-world engineering scenarios, as it employs universally applicable techniques such as information gain calculation, evaluation of monitoring system performance through Bayesian inference, and modelling of sensor network failures. The case studies presented serve as illustrations of this methodology, which do not limit its applicability. For instance, the application of Bayesian inference for defect localization in two different skin panels with irregular geometries on aircraft wings [17] exemplifies a direct extension of this methodology for evaluating reliability in practical situations.

6. Conclusions

This paper presents a comprehensive methodology for assessing the reliability of SHM systems throughout their operational lifespan. This approach combines PN to simulate sensor failures and EIG calculations to quantify the impact on monitoring accuracy and uncertainty. The PN module generates sequences of sensor failures, while the EIG metric is demonstrated to effectively capture changes in monitoring accuracy and uncertainty through a quadratic equation. Monitoring accuracy and uncertainty are determined through physics-based Bayesian inference for ultrasonic localization and identification. The proposed methodology is rigorously validated through both numerical simulations and experimental tests using an ultrasonic monitoring system. Importantly, this approach can be readily extended to assess the reliability of various monitoring systems, particularly those vulnerable to sensor failures. The following conclusions are drawn from this paper:

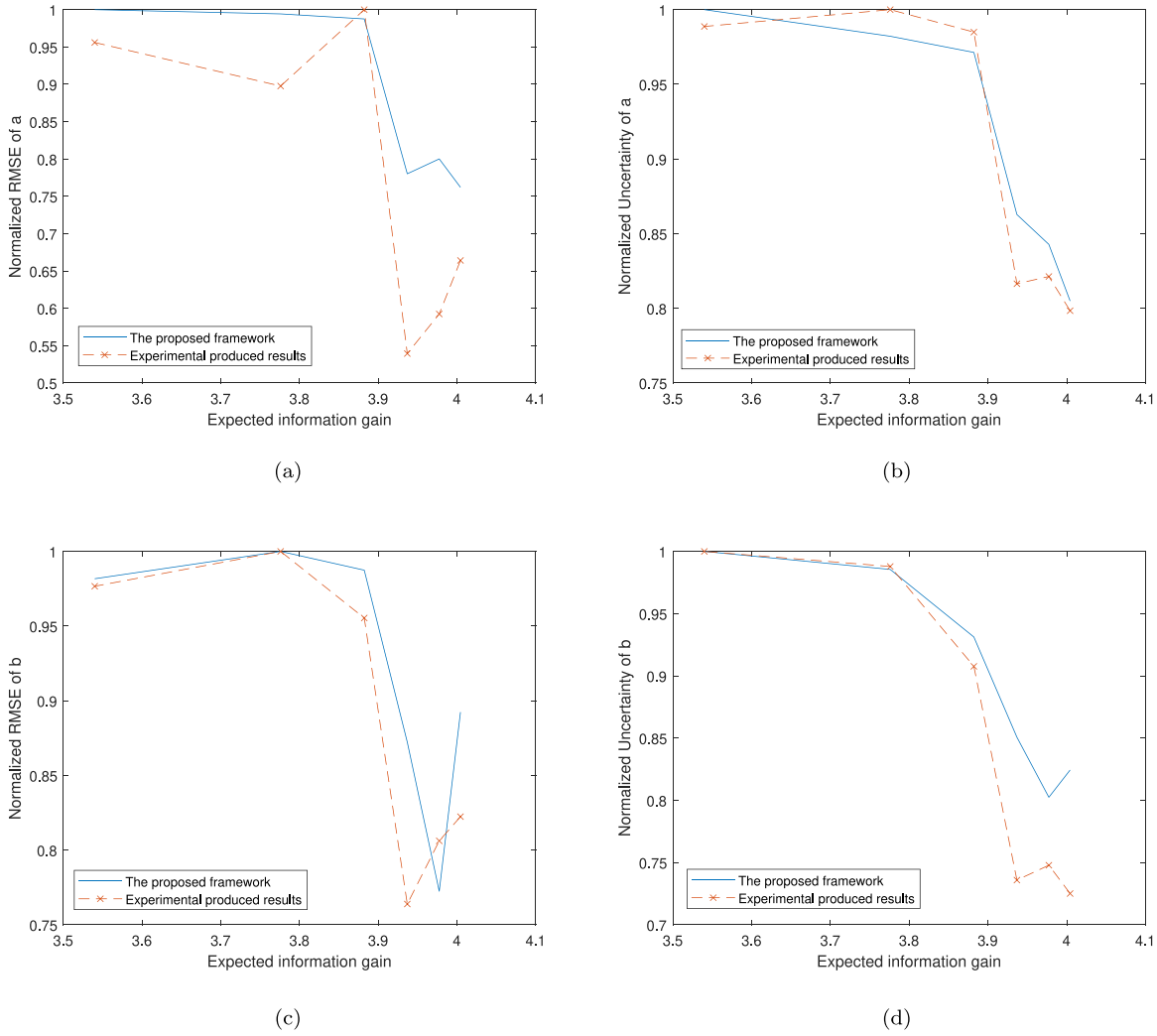

Fig. 15. (a) RMSE of a, (b) uncertainty of a, (c) RMSE of b and (d) uncertainty of b verified by the physical experiment.

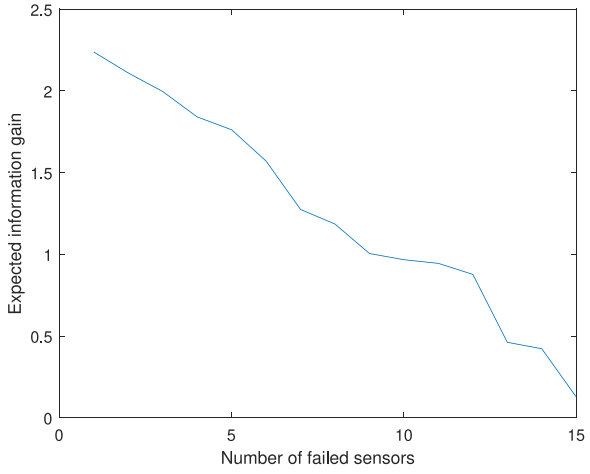

Fig. 16. EIG with the increase of failed sensors in terms of damage localization.

- The proposed framework for evaluating SHM reliability, considering sensor failures, has the capability to generate a single value that reflects the reliability in sizing and localizing the detected damage.
- Errors in the monitoring process may change as external conditions change, which will bring different uncertainties. Changes in reliability indicator values can reflect varying degrees of uncertainty.
- By combining the PN to simulate the monitoring system degradation, and the EIG to estimate of reliability, the proposed framework can predict the changes in monitoring accuracy and uncertainty within the lifetime of the monitoring system.

The current Bayesian inference framework requires the selection of likelihood function format, which may have issues with convergence when levels of uncertainty are large. Approximate Bayesian computation (ABC) can avoid the formulation of the likelihood function [45]. Future work is considered to include ABC in the proposed approach. And possible to apply and validate it in other SHM applications, such as vibration-based methods. Another area for improvement involves expanding the information modelling to incorporate random measurement errors, bias, and signal errors caused by the operational environment. Furthermore, it is necessary to investigate the use of

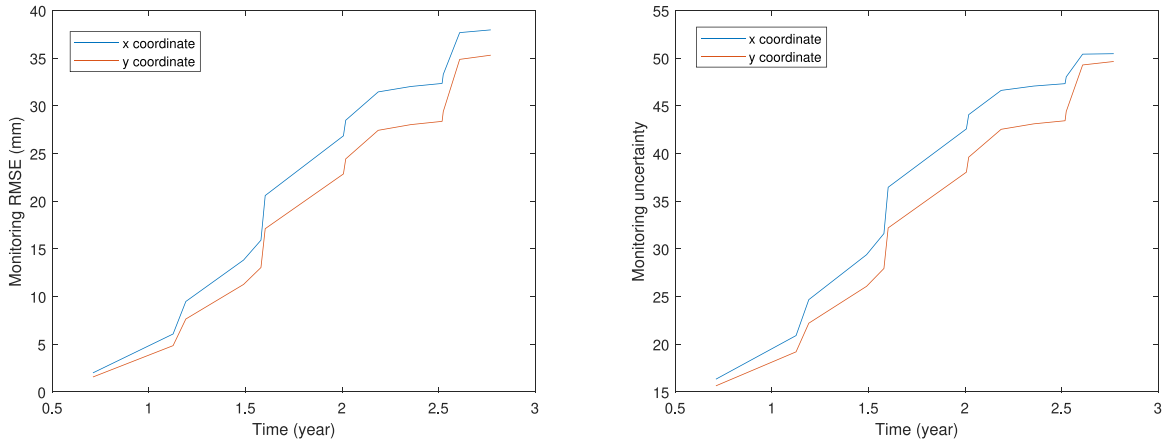

Fig. 17. (a) Monitoring RMSE, (b) uncertainty of damage coordinates over time in terms of damage localization.

the proposed reliability analysis method to address damage detection problems (PoD development) in future research.

CRediT authorship contribution statement

Wen Wu: Writing – original draft, Visualization, Validation, Software, Methodology, Formal analysis, Conceptualization. **Sergio Cantero-Chinchilla:** Writing – review & editing, Validation, Supervision, Software, Formal analysis, Conceptualization. **Darren Prescott:** Writing – review & editing, Supervision, Investigation, Conceptualization. **Rasa Remenyte-Prescott:** Writing – review & editing, Supervision, Project administration, Funding acquisition, Conceptualization. **Manuel Chiachío:** Writing – review & editing, Supervision, Investigation.

Declaration of competing interest

The authors declare that they have no known competing financial interests or personal relationships that could have appeared to influence the work reported in this paper.

Data availability

Data will be made available on request.

Acknowledgements

This work has received funding from the European Union's Horizon 2020 research and innovation program under the Marie Skłodowska-Curie grant agreement No. 859957.

References

[1] Farrar CR, Worden K. An introduction to structural health monitoring. Phil Trans R Soc A 2007;365(1851):303–15.
[2] Duan C, Deng T, Song L, Wang M, Sheng B. An adaptive reliability-based maintenance policy for mechanical systems under variable environments. Reliab Eng Syst Saf 2023;238:109396.
[3] Saberzadeh Z, Razmkhah M, Amini M. Bayesian reliability analysis of complex k-out-of-n: systems under degradation performance. Reliab Eng Syst Saf 2023;231:109020.
[4] Zhao X, Guo B, Chen Y. A condition-based inspection-maintenance policy for critical systems with an unreliable monitor system. Reliab Eng Syst Saf 2024;242:109710.
[5] Falcetelli F, Yue N, Di Sante R, Zarouchas D. Probability of detection, localization, and sizing: The evolution of reliability metrics in structural health monitoring. Struct Health Monit 2022;21(6):2990–3017.
[6] Gianneo A, Carboni M, Giglio M. A preliminary study of multi-parameter POD curves for a guided waves based SHM approach to lightweight materials. In: AIP conference proceedings. Vol. 1706, AIP Publishing LLC; 2016, 030018.
[7] Tschöke K, Mueller I, Memmolo V, Moix-Bonet M, Moll J, Lugovtsova Y, Golub M, Venkat RS, Schubert L. Feasibility of model-assisted probability of detection principles for structural health monitoring systems based on guided waves for fiber-reinforced composites. IEEE Trans Ultrason Ferroelectr Freq Control 2021;68(10):3156–73.
[8] Pado L, Ihn J, Dunne J. Understanding probability of detection (POD) in structure health monitoring systems. Struct Health Monit 2013. 2013.
[9] Aldrin JC, Annis C, Sabbagh HA, Lindgren EA. Best practices for evaluating the capability of nondestructive evaluation (NDE) and structural health monitoring (SHM) techniques for damage characterization. In: AIP conference proceedings. 1706, (1). AIP Publishing; 2016.
[10] Zhang W-H, Qin J, Lu D-G, Liu M, Faber MH. Quantification of the value of condition monitoring system with time-varying monitoring performance in the context of risk-based inspection. Reliab Eng Syst Saf 2023;231:108993.
[11] Falcetelli F, Cristiani D, Yue N, Sbarufatti C, Troiani E, Di Sante R, Zarouchas D. Qualification of distributed optical fiber sensors using probability of detection curves for delamination in composite laminates. Struct Health Monit 2023;22(5):2972–86.
[12] Zhang W-H, Qin J, Lu D-G, Liu M, Faber MH. Quantifying the value of structural health monitoring information with measurement bias impacts in the framework of dynamic Bayesian Network. Mech Syst Signal Process 2023;187:109916.
[13] Kamariotis A, Chatzi E, Straub D. A framework for quantifying the value of vibration-based structural health monitoring. Mech Syst Signal Process 2023;184:109708.
[14] Thomas M, Joy AT. Elements of information theory. Wiley-Interscience; 2006.
[15] Argyris C, Chowdhury S, Zabel V, Papadimitriou C. Bayesian optimal sensor placement for crack identification in structures using strain measurements. Struct Control Health Monit 2018;25(5):e2137.
[16] Cantero-Chinchilla S, Chiachío J, Chiachío M, Chronopoulos D, Jones A. Optimal sensor configuration for ultrasonic guided-wave inspection based on value of information. Mech Syst Signal Process 2020;135:106377.
[17] Cantero-Chinchilla S, Beck JL, Chiachío M, Chiachío J, Chronopoulos D, Jones A. Optimal sensor and actuator placement for structural health monitoring via an efficient convex cost-benefit optimization. Mech Syst Signal Process 2020;144:106901.
[18] Cantero-Chinchilla S, Papadimitriou C, Chiachío J, Chiachío M, Koumoutsakos P, Fabro AT, Chronopoulos D. Robust optimal sensor configuration using the value of information. Struct Control Health Monit 2022;29(12):e3143.
[19] Mukhopadhyay K, Liu B, Bedford T, Finkelstein M. Remaining lifetime of degrading systems continuously monitored by degrading sensors. Reliab Eng Syst Saf 2023;231:109022.
[20] Yan R, Dunnett S, Andrews J. A Petri net model-based resilience analysis of nuclear power plants under the threat of natural hazards. Reliab Eng Syst Saf 2023;230:108979.
[21] Yan R, Dunnett SJ, Jackson LM. Model-based research for aiding decision-making during the design and operation of multi-load automated guided vehicle systems. Reliab Eng Syst Saf 2022;219:108264.
[22] Naybour M, Remenyte-Prescott R, Boyd MJ. Reliability and efficiency evaluation of a community pharmacy dispensing process using a coloured Petri-net approach. Reliab Eng Syst Saf 2019;182:258–68.
[23] Andrews J. A modelling approach to railway track asset management. Proc Inst Mech Eng F: J Rail Rapid Transit 2013;227(1):56–73.

[24] Le B, Andrews J. Modelling wind turbine degradation and maintenance. Wind Energy 2016;19(4):571–91.
[25] Saleh A, Chiachío M, Salas JF, Kolios A. Self-adaptive optimized maintenance of offshore wind turbines by intelligent Petri nets. Reliab Eng Syst Saf 2023;231:109013.
[26] Murata T. Petri nets: Properties, analysis and applications. Proc IEEE 1989;77(4):541–80.
[27] Wu W, Saleh A, Remenyte-Prescott R, Prescott D, Chiachio M, Chronopoulos D. Asset management modelling approach integrating structural health monitoring data for composite components of wind turbine blades. In: Proceedings of the 32nd European safety and reliability conference (ESREL 2022). Research Publishing Services; 2022.
[28] Burnham KP, Anderson DR. Practical use of the information-theoretic approach. In: Model selection and inference. Springer; 1998, p. 75–117.
[29] Cantero-Chinchilla S, Chiachío J, Chiachío M, Chronopoulos D, Jones A. A robust Bayesian methodology for damage localization in plate-like structures using ultrasonic guided-waves. Mech Syst Signal Process 2019;122:192–205.
[30] Su Z, Ye L. Identification of damage using Lamb waves: from fundamentals to applications, Vol. 48, Springer Science & Business Media; 2009.
[31] Beck JL. Bayesian system identification based on probability logic. Struct Control Health Monit 2010;17(7):825–47.
[32] Jaynes ET. Information theory and statistical mechanics. Phys Rev 1957;106(4):620.
[33] Qin J. Preposterior analysis considering uncertainties and dependencies of information relevant to structural performance. ASCE-ASME J Risk Uncertain Eng Syst A 2022;8(1):04021085.
[34] Ali K, Qin J, Faber MH. On information modeling in structural integrity management. Struct Health Monit 2022;21(1):59–71.
[35] Metropolis N, Rosenbluth AW, Rosenbluth MN, Teller AH, Teller E. Equation of state calculations by fast computing machines. J Chem Phys 1953;21(6):1087–92.
[36] Hastings WK. Monte Carlo sampling methods using Markov chains and their applications. Oxford University Press; 1970.
[37] Chiachío M, Chiachío J, Rus G, Beck JL. Predicting fatigue damage in composites: A Bayesian framework. Struct Saf 2014;51:57–68.
[38] Gelman A, Gilks W, Roberts G. Efficient Metropolis jumping rules, Vol. 5, Oxford: Oxford University Press; 1996.
[39] Roberts GO, Rosenthal JS. Optimal scaling for various Metropolis-Hastings algorithms. Stat Sci 2001;16(4):351–67.
[40] Izquierdo K, Lekić V, Montési LG. A Bayesian approach to infer interior mass anomalies from the gravity data of celestial bodies. Geophys J Int 2020;220(3):1687–99.
[41] Malinverno A. Parsimonious Bayesian Markov chain Monte Carlo inversion in a nonlinear geophysical problem. Geophys J Int 2002;151(3):675–88.
[42] ABAQUS. Abaqus documentation. Providence, RI, USA: Dassault Systèmes; 2016.
[43] Wu W, Malik M, Cantero-Chinchilla S, Lawrie T, Yan W, Tanner G, Remenyte-Prescott R, Chronopoulos D. Guided waves-based damage identification in plates through an inverse Bayesian process. Ultrasonics 2022;106773.
[44] Grahn T. Lamb wave scattering from a circular partly through-thickness hole in a plate. Wave Motion 2003;37(1):63–80.
[45] Chiachio M, Beck JL, Chiachio J, Rus G. Approximate Bayesian computation by subset simulation. SIAM J Sci Comput 2014;36(3):A1339–58.